

TiO₂-Coated Interlayer-Expanded MoSe₂/Phosphorus-Doped Carbon Nanospheres for Ultrafast and Ultralong Cycling Sodium Storage

Yuyu Wang, Yunxiao Wang, Wenpei Kang,* Dongwei Cao, Chenxu Li, Dongxu Cao, Zixi Kang, Daofeng Sun,* Rongming Wang, and Yuliang Cao*


Based on multielectron conversion reactions, layered transition metal dichalcogenides are considered promising electrode materials for sodium-ion batteries, but suffer from poor cycling performance and rate capability due to their low intrinsic conductivity and severe volume variations. Here, interlayer-expanded MoSe₂/phosphorus-doped carbon hybrid nanospheres coated by anatase TiO₂ (denoted as MoSe₂/P-C@TiO₂) are prepared by a facile hydrolysis reaction, in which TiO₂ coating polypyrrole-phosphomolybdic acid is utilized as a novel precursor followed by a selenization process. Benefiting from synergistic effects of MoSe₂, phosphorus-doped carbon, and TiO₂, the hybrid nanospheres manifest unprecedented cycling stability and ultrafast pseudocapacitive sodium storage capability. The MoSe₂/P-C@TiO₂ delivers decent reversible capacities of 214 mAh g⁻¹ at 5.0 A g⁻¹ for 8000 cycles, 154 mAh g⁻¹ at 10.0 A g⁻¹ for 10000 cycles, and an exceptional rate capability up to 20.0 A g⁻¹ with a capacity of ≈175 mAh g⁻¹ in a voltage range of 0.5–3.0 V. Coupled with a Na₃V₂(PO₄)₃@C cathode, a full cell successfully confirms a reversible capacity of 242.2 mAh g⁻¹ at 0.5 A g⁻¹ for 100 cycles with a coulombic efficiency over 99%.

1. Introduction

Sodium-ion batteries (SIBs) possessing a similar structure characteristics and energy storage mechanism to those of lithium-ion batteries (LIBs), serving as one of the most promising energy-storage devices, have attracted our tremendous attention on account of their low cost, abundant, and widespread sodium resources.^[1–4] Nevertheless, the large ionic radius of an Na⁺ ion (≈1.09 Å), which is 55% larger than that of Li⁺ ion, and its higher molar mass make the sodiation/desodiation kinetics more sluggish, impeding the development and practical application of SIBs.^[5–7] For these reasons, numerous effort including development of appropriate anode materials has been taken to satisfy the demands of decent specific capacity, long cycle life, and excellent rate performance for stationary energy storage.^[8–10]

MoSe₂, a representative type of layered transition metal dichalcogenide (TMD) material, exhibits high theoretical capacity, large interlayer spacing, and small bandgap, and thus has been proved to be a good candidate anode material for SIBs.^[11–15] Unfortunately, it still suffers from rapid cycling capacity degradation caused by large volume change and slow kinetics during the sodiation/desodiation process. According to previous research,^[16–19] construction of rational nanostructures and formation of carbon-based composites are effective approaches. Various nanostructures, including MoSe₂@porous hollow carbon spheres,^[20] carbon-stabilized interlayer-expanded MoSe₂ nanosheets,^[21] and fullerene-like MoSe₂ nanoparticles-embedded CNT balls,^[22] have been explored to enhance the electrochemical performance of MoSe₂. On the other hand, the interlayer-expanded structures are very critical, which can provide efficient ion migration channels, facilitating to enhance charge/discharge kinetics. Sun's group successfully synthesized interlayer-expanded MoSe₂@hollow carbon nanosphere (HCNS) materials, which exhibited a specific capacity of 471 mAh g⁻¹ after 1000 cycles at 3.0 A g⁻¹.^[23] These results confirm that sodium storage performance can be enhanced through rational nanostructure engineering. However, in view

Y. Y. Wang, Dr. W. P. Kang, D. W. Cao, C. X. Li, D. X. Cao,
Dr. Z. X. Kang, Prof. D. F. Sun, Prof. R. M. Wang
College of Science
School of Materials Science and Engineering
China University of Petroleum (East China)
Qingdao, Shandong 266580, P. R. China
E-mail: wpkang@upc.edu.cn; dfsun@upc.edu.cn
Dr. Y. X. Wang, Prof. Y. L. Cao
College of Chemistry and Molecular Sciences
Hubei Key Laboratory of Electrochemical Power Sources
Wuhan University
Wuhan 430072, P. R. China
E-mail: ylcao@whu.edu.cn

 The ORCID identification number(s) for the author(s) of this article can be found under <https://doi.org/10.1002/adv.201801222>.

© 2018 The Authors. Published by WILEY-VCH Verlag GmbH & Co. KGaA, Weinheim. This is an open access article under the terms of the Creative Commons Attribution License, which permits use, distribution and reproduction in any medium, provided the original work is properly cited.

DOI: 10.1002/adv.201801222

of the long cycle life for practical applications, the serious volume changes during charge and discharge processes remain challenging and need to be further alleviated.

As one of the typical insertion-type electrode materials for secondary batteries, TiO_2 possesses reasonable insertion potential and negligible change in volume, showing good structural stability and long cycle life.^[24–29] Although its theoretical specific capacity is fairly low, it can serve as an effective protective layer for other electrode materials with severe volume expansion, such as metal oxides or metal sulfides through smart hybridization.^[30–35] Such an approach can effectively ensure the specific capacity and achieve a long cycle life attributed to that the rigid TiO_2 layer could tolerate the interior volume variation of metal oxides or metal sulfides. For instance, Wang and co-workers reported porous hollow $\alpha\text{-Fe}_2\text{O}_3@ \text{TiO}_2$ core-shell nanospheres.^[30] When used as anode materials in SIBs, these hybrid hierarchical nanospheres delivered a high reversible capacity of 267 mAh g^{-1} at 100 mA g^{-1} with an excellent cycling stability up to 300 cycles.

In this work, we report an elaborate anode, consisted of interlayer-expanded MoSe_2 /phosphorus-doped carbon nanospheres composite and anatase TiO_2 coating (denoted as $\text{MoSe}_2/\text{P-C}@ \text{TiO}_2$). In a facile hydrolysis reaction in acidic medium, TiO_2 layer was coated on PPy- PMo_{12} precursor nanospheres, followed by a confined selenization process, $\text{MoSe}_2/\text{P-C}@ \text{TiO}_2$ nanospheres can be obtained by inheriting the morphology of the PPy- PMo_{12} precursor. Compared to previous reports on MoSe_2 -based composite electrodes, our MoSe_2 -based hybrid has the following advantages: (i) the phosphorus-doped carbon transformed from the PPy- PMo_{12} precursor, can increase the conductivity of nanocomposite and provide more active sites between Na^+ and the electrolyte to improve the charge transfer efficiency; (ii) the expanded interlayer spacing of MoSe_2 can decrease the ion diffusion resistance and facilitate the fast Na^+ insertion/extraction reaction kinetics; (iii) the coated TiO_2 layer plays an essential role in alleviating the volume changes upon sodiation/desodiation process, thus preserving the electrode integrity; and (iv) the synergistic effect of MoSe_2 , phosphorus-doped carbon, and TiO_2 can enhance the electrochemical performance for SIBs. Benefiting from the unique configuration of the as-fabricated $\text{MoSe}_2/\text{P-C}@ \text{TiO}_2$ nanospheres, when used as an anode material for SIBs, it exhibits ultralong cycle stability, superior specific capacity, and exceptional rate capability. Additionally, this hybrid structure manifests a relatively small irreversible capacity loss with a high initial coulombic efficiency (ICE) of 81.3%, which further enable it a feasible anode for practical full cells.

2. Results and Discussion

The synthesis process of $\text{MoSe}_2/\text{P-C}@ \text{TiO}_2$ nanospheres is schematically illustrated in **Figure 1A**. Briefly, the uniform PPy- PMo_{12} nanospheres are first synthesized through a polymerization reaction of phosphomolybdic acid and pyrrole forming polypyrrole-phosphomolybdic acid (PPy- PMo_{12}). Then a layer of TiO_2 nanoparticles is grown on the PPy- PMo_{12} nanospheres through a deposition process in chemical bath. Finally, $\text{MoSe}_2/\text{P-C}@ \text{TiO}_2$ nanospheres are successfully obtained after

calcination with Se powder in a tube furnace. To estimate the influence of P-C and TiO_2 coating, $\text{MoSe}_2/\text{P-C}$ and $\text{MoSe}_2@ \text{TiO}_2$ composites were also prepared following a similar process.

Figure 1B shows the X-ray diffraction (XRD) patterns of as-obtained $\text{MoSe}_2/\text{P-C}$, TiO_2 , and $\text{MoSe}_2/\text{P-C}@ \text{TiO}_2$ nanospheres. The diffraction peaks at 25.28°, 37.80°, 48.05°, and 62.68° can be assigned to (101), (004), (200), and (204) planes of anatase TiO_2 (JCPDS No. 21-1272). Three characteristic peaks at 31.42°, 37.88°, and 55.92° are consistent with the planes of (100), (103), and (110) for the hexagonal MoSe_2 phase (JCPDS No. 29-0914). In addition, a peak at $\approx 7.04^\circ$ can be observed, which corresponds to expanded (002) plane, exhibiting an obvious shift of 6.66° compared with the JCPDS data. According to the Bragg equation, the interlayer spacing is calculated to be 1.26 nm, indicating formation of an expanded interlayer, which may be attributed to the intercalation of in situ carbon between the interlayers^[23,36] during the PPy- PMo_{12} precursor calcination with Se powder at 700 °C. Raman spectra were used to further characterize the MoSe_2 , TiO_2 , and carbon materials in the composite. In Raman spectrum of the $\text{MoSe}_2/\text{P-C}@ \text{TiO}_2$ (**Figure 1C**), there are two weak peaks at ≈ 395 and 515 cm^{-1} , which symbolize the B_1^g and A_1^g modes of the anatase phase of the TiO_2 .^[37] Meanwhile, a strong peak at 237.6 cm^{-1} is the A_1^g mode originating from the out-of-plane vibration of the Mo–Se band and another peak at ≈ 289.8 cm^{-1} belongs to the E_{2g}^1 mode originating from the Mo–Se in-plane vibration.^[14,19] Compared to the $\text{MoSe}_2/\text{P-C}$, slight shifts of the corresponding peaks occurred due to the surface strain that may be caused by the TiO_2 coating.^[38] In addition, two peaks around 1360 and 1591 cm^{-1} are observed, corresponding to the D band for defected and disordered carbon and the G band derived from the vibration of sp^2 carbon atoms, respectively.^[14,19,39] The I_D/I_G intensity ratio is 0.92, higher than 0.90 in the $\text{MoSe}_2/\text{P-C}$, indicating a more defected and disordered structure in the carbon component of $\text{MoSe}_2/\text{P-C}@ \text{TiO}_2$.^[39] As roughly verified by thermogravimetric analysis (TGA), as shown in **Figure 1D**, the mass contents of carbon, MoSe_2 , and TiO_2 in the composite are 15.11, 74.36, and 10.53%, respectively. And the detailed calculating process is added in the Supporting Information. Moreover, the $\text{MoSe}_2/\text{P-C}@ \text{TiO}_2$ nanospheres exhibit a specific Brunauer–Emmett–Teller (BET) surface area of 14.18 $\text{m}^2 \text{g}^{-1}$ (**Figure 1E**), suggesting there are sufficient active sites for the electrolyte contact when used as anode material in SIBs.

Field emission scanning electron microscope (FESEM) and transmission electron microscope (TEM) images offer insights into the morphology and microstructure of the product. A panoramic view of the product (**Figure 2A**) indicates that it is composed of uniform nanospheres with size ≈ 100 nm, which is consistent with the PPy- PMo_{12} precursor and $\text{MoSe}_2/\text{P-C}$ (**Figure S1**, Supporting Information). This result reveals that the $\text{MoSe}_2/\text{P-C}@ \text{TiO}_2$ can still maintain the nanosphere without any aggregation or collapse after TiO_2 coating and even high-temperature calcination. Compared with the smooth surface of the PPy- PMo_{12} precursor and $\text{MoSe}_2/\text{P-C}$, the $\text{MoSe}_2/\text{P-C}@ \text{TiO}_2$ possesses a rough surface with assembled nanoparticles (**Figure 2B**), suggesting the successful coating of the TiO_2 layer. It should be noted that the agglomeration of $\text{MoSe}_2@ \text{TiO}_2$ occurs (**Figure S2**, Supporting Information), indicating the importance of in situ P–C on the sphere structure

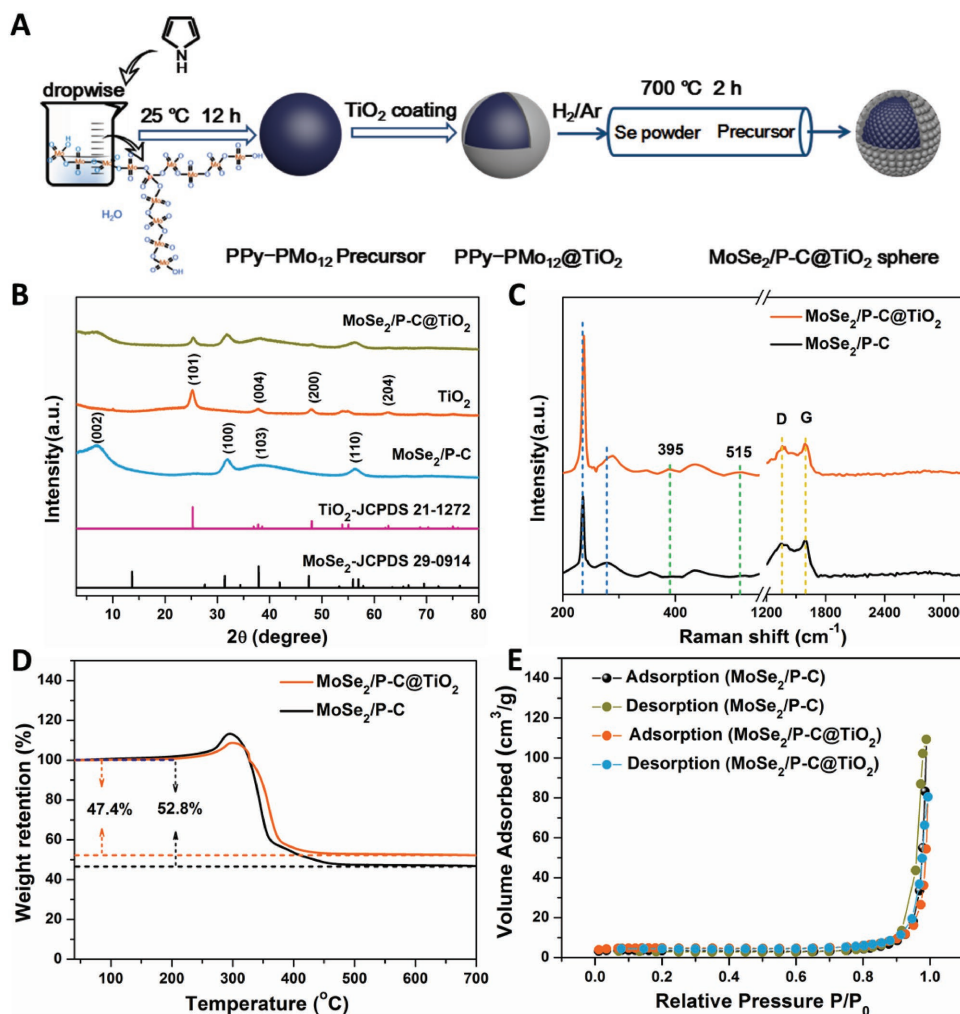


Figure 1. A) Schematic illustration of the synthesis process for the spherical MoSe₂/P-C@TiO₂ nanocomposite. B) XRD patterns. C) Raman spectra. D) TGA curves. E) N₂ adsorption/desorption isotherm of MoSe₂/P-C@TiO₂ hybrid nanospheres and MoSe₂/P-C nanospheres.

preservation. As can be seen from Figure 2C, the layered structure and well-defined TiO₂ layers on the surface of the nanospheres can be clearly observed in the low-magnification TEM image. A typical high-resolution TEM (HRTEM) image is shown in Figure 2D, from which the expanded (002) lattice spacing (≈ 1.26 nm) of MoSe₂ can be clearly observed and is consistent with the XRD results. The increased interlayer spacing means lower ion diffusion resistance and more available and accessible active surface area, promoting the rate capability when used as an SIB anode.^[19,40] Besides, two distinct lattice fringes at the edge of nanospheres with spacings of 0.35 and 0.23 nm can be observed, respectively, in well agreement with the (101) and (112) planes of anatase TiO₂. The selected-area electron diffraction (SAED) pattern (Figure 2E) shows multiple diffraction rings, confirming the formation of a polycrystalline structure. As shown in Figure 2F–L and Figure S3 (Supporting Information), the high-angle annular dark-field scanning TEM (HAADF-STEM) image and the corresponding energy-dispersive X-ray spectrum (EDX) elemental mappings unambiguously identify the Mo, Se, C, and P elements covering the entire spherical structure, while Ti and O elements

are mainly dispersed on the surface of the sphere, revealing that the architecture has ingeniously integrated features of the hybrid nanostructures.

X-ray photoelectron spectroscopy (XPS) spectra (Figure 3) were recorded to further examine the surface information and oxidation states of the chemical elements in the MoSe₂/P-C@TiO₂ nanospheres. Six elements, Mo, Se, Ti, O, C, and P, can be clearly seen from the survey spectrum in Figure S4 (Supporting Information). The Mo 3d core level spectrum is shown in Figure 3A, which can be fitted into four peaks at 227.8, 230.9, 232.6, and 235.5 eV. The characteristic peaks at 227.8 and 230.9 eV can be attributed to Mo⁴⁺ 3d_{3/2} and Mo⁴⁺ 3d_{5/2}, respectively.^[23] In addition, the peaks at 232.6 and 235.5 eV represent the appearance of Mo⁶⁺ due to the partial oxidation of MoSe₂.^[41] In the Se 3d spectrum (Figure 3B), there are two peaks located at 53.1 and 54.0 eV, which are assigned, respectively, to the Se 3d_{5/2} and Se 3d_{3/2}.^[42] Figure 3C depicts the Ti 2p core level spectrum with two peaks centered at 458.1 eV for Ti 2p_{3/2} and 463.9 eV for Ti 2p_{1/2}.^[43] The distance between the Ti 2p_{1/2} and Ti 2p_{3/2} core levels is 5.8 eV, suggesting a normal state of Ti⁴⁺ in the anatase TiO₂.^[33,44] As shown in the O 1s

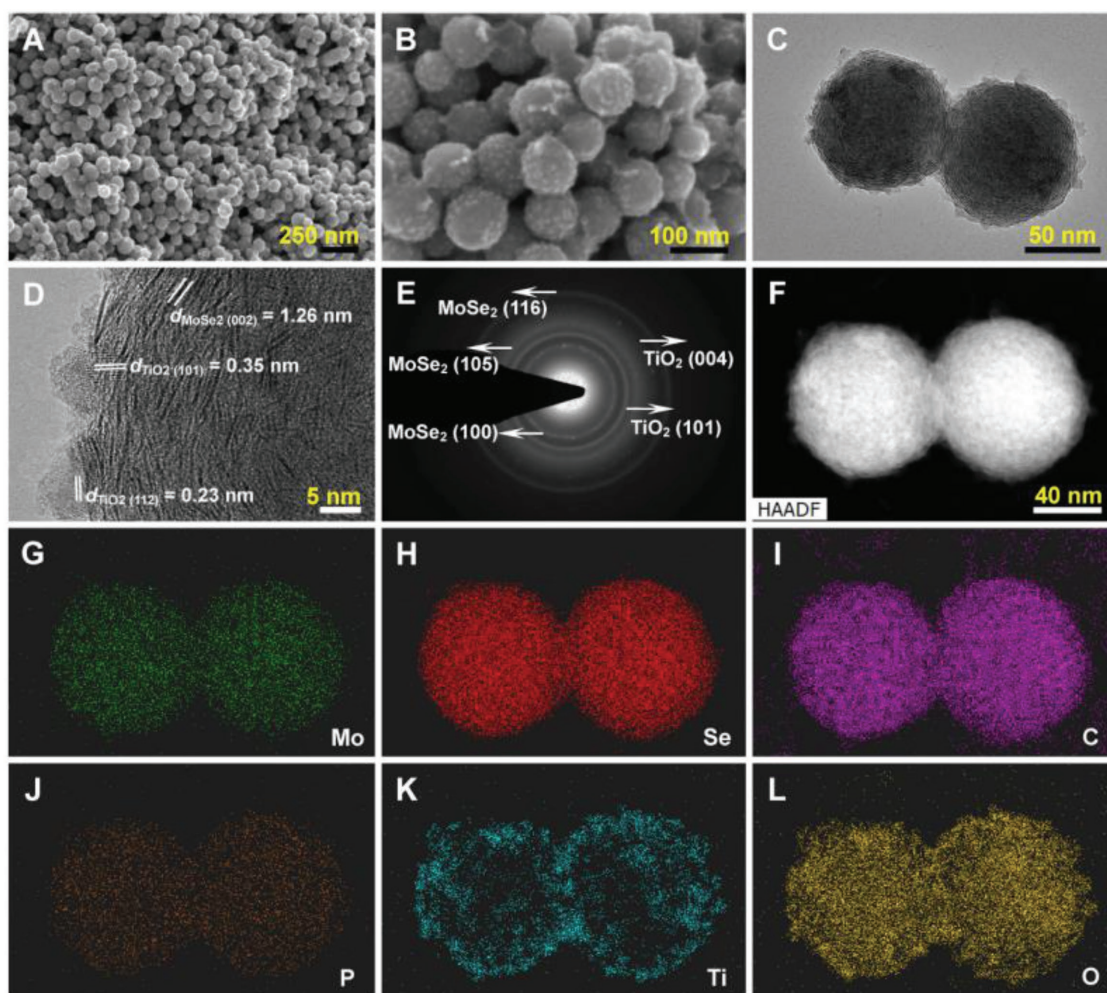


Figure 2. Morphology and structure of the $\text{MoSe}_2/\text{P-C}@/\text{TiO}_2$ hybrid nanospheres. A,B) FESEM images. C) TEM images. D) HRTEM image. E) The corresponding SAED pattern. F–L) HAADF-STEM image and the corresponding EDX mappings of Mo, Se, C, P, Ti, and O. The scale bar in (F) also applies to (G)–(L).

spectrum (Figure 3D), the binding energy of Ti–O, O–H, and H_2O is observed at 529.8, 531.9, and 533.8 eV, respectively.^[45,46] These results indicate the successful coating of the anatase TiO_2 phase. The XPS spectrum of the P 2p core-level (Figure 3E) displays two peaks at 133.0 and 135.1 eV, which are related to P–C and P=O bonds, respectively.^[11,47] The C 1s spectrum (Figure 3F) could be divided into three peaks, which are located at 284.3, 285.1, and 285.7 eV, corresponding to sp^2 C, sp^3 C, and C–P bonds, respectively.

The successful synthesis of the $\text{MoSe}_2/\text{P-C}@/\text{TiO}_2$ hybrid nanospheres for a superior SIB anode material is confirmed from the excellent electrochemical behavior (Figure 4). Figure 4A shows the cyclic voltammetry (CV) curves of $\text{MoSe}_2/\text{P-C}@/\text{TiO}_2$ anode in a voltage range of 0.5–3.0 V versus Na/Na^+ at a scan rate of 0.1 mV s^{-1} for the initial five cycles. During the first discharge process, three main cathodic peaks at 1.53, 0.60, and 0.50 V can be observed. Compared with CV curves of the $\text{MoSe}_2/\text{P-C}$ and TiO_2 (Figure S5, Supporting Information), the peak at 1.53 V corresponds to the Na^+ intercalation into anatase TiO_2 phase.^[48] The reduction peak at 0.60 eV can be attributed to the Na^+ insertion into the interlayer of MoSe_2

and formation of Na_xMoSe_2 , and the other peak at 0.50 eV is assigned to conversion reaction from Na_xMoSe_2 to Mo metal and Na_2Se with the formation of a solid electrolyte interphase (SEI) layer.^[23,49] Accordingly, the oxidation peaks at 1.67 and 2.10 V are associated with the oxidation of Mo to MoSe_2 and Na_xTiO_2 to TiO_2 , respectively. After the first cycle, the following CV curves are almost overlapped and the reduction peaks move to higher potential, indicating the good reversibility of $\text{MoSe}_2/\text{P-C}@/\text{TiO}_2$ anode during the repeated sodiation/desodiation processes. The main peak locating at 1.38 V should be attributed to the reactions of Na^+ insertion, the interlayer of MoSe_2 , and subsequent reduction into Mo and Na_2Se .

Figure 4B exhibits the galvanostatic discharge–charge curves of $\text{MoSe}_2/\text{P-C}@/\text{TiO}_2$ composite electrode at 5.0 A g^{-1} in the voltage range of 0.5–3.0 V, which are well consistent with the CV results. The initial charge and discharge capacities are ≈ 293.3 and 360.8 mAh g^{-1} , respectively, giving an ICE of 81.3%. As the cycles proceed, the charge and discharge capacities from 10th to 100th cycles show a trend of decrease followed by a slight increase in subsequent cycles. This result is further demonstrated by a galvanostatic charge–discharge

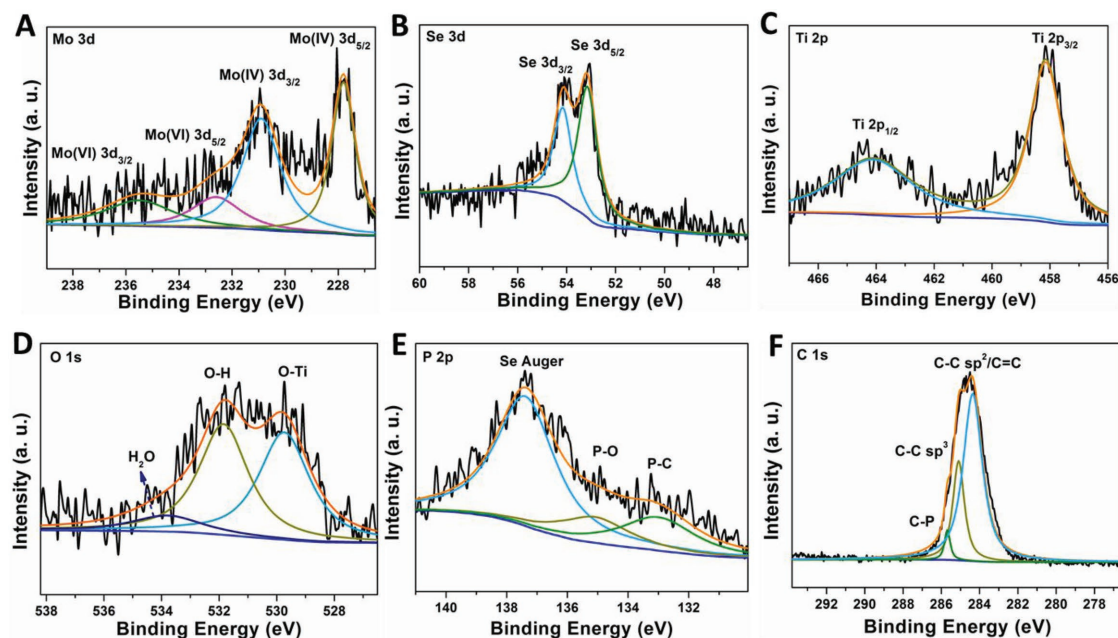


Figure 3. XPS spectra of the $\text{MoSe}_2/\text{P-C}@/\text{TiO}_2$ composite. A–F) High-resolution XPS spectra for Mo 3d, Se 3d, Ti 2p, O 1s, P 2p, and C 1s.

cycling test, as shown in Figure 4C,D. The reversible discharge capacities for the 500th, 800th, and 1000th cycles are 214, 223, and 229 mAh g^{-1} with average CEs up to $\approx 100\%$, showing an outstanding cycling stability. The cycling performance of the $\text{MoSe}_2/\text{P-C}$ and TiO_2 is also carried out at the current of 5.0 A g^{-1} (Figure 4C), which clearly demonstrates the effects of the TiO_2 modified $\text{MoSe}_2/\text{P-C}$ in improving the sodium storage performance. It is found that although the reversible capacity of TiO_2 is noticeably low in the voltage range of 0.5–3.0 V, its cycling stability is clearly better than the other two materials. The $\text{MoSe}_2/\text{P-C}$ electrode shows higher discharge capacities than those of $\text{MoSe}_2/\text{P-C}@/\text{TiO}_2$ in the initial 40 cycles. After 40 cycles, it exhibits a rapid decrease and stabilizes the discharge capacity of only 138 mAh g^{-1} after 8000 cycles with a low capacity retention of 50.7% in comparison with the value for the second cycle. And the capacities of $\text{MoSe}_2@/\text{TiO}_2$ are lower and a capacity of 60.5 mAh g^{-1} can be maintained after 8000 cycles. In contrast, the reversible capacity of $\text{MoSe}_2/\text{P-C}@/\text{TiO}_2$ electrode decreases slightly in the initial 243 cycles because of the polarization when cycled at high current and delivers a little increase capacity attributed to progressive kinetic activation in the electrode.^[12,31,40,48] After those, a stable capacity of 214 mAh g^{-1} can be delivered after 8000 cycles, giving a capacity retention of 82.9%. This result indicates that $\text{MoSe}_2/\text{P-C}@/\text{TiO}_2$ electrode, as expected, exhibits a synthetic effect combining the advantages for the individual components. Moreover, long cycling life can be verified as shown in Figure 4D. Even at a high current density of 10.0 A g^{-1} , the discharge capacity of 154 mAh g^{-1} can be maintained over 10 000 cycles with CEs as high as 100%, delivering a capacity retention of 68.1%.

As expected, the $\text{MoSe}_2/\text{P-C}@/\text{TiO}_2$ hybrid electrode manifests an excellent high rate capability, as indicated in Figure 4E. At current densities of 0.1, 0.2, 0.5, 1.0, 2.0, and 5.0 A g^{-1} , the reversible capacities of the hybrid nanospheres are ≈ 270 , 250, 240, 236, 228, and 214 mAh g^{-1} , respectively. Even at the

high current densities of 10.0 and 20.0 A g^{-1} , the hybrid can still deliver capacities as high as 202 and 175 mAh g^{-1} , respectively. This high-rate sodium-storage capability exceeds those of many other $\text{MoS}_2/\text{MoSe}_2$ -based nanostructures such as MoS_2/C nanotube, MoS_2/C hybrid, MoS_2 nanoflowers, PEO- MoS_2 nanocomposites, C- MoSe_2/rGO composite, and few-layered and carbon-modified MoSe_2 nanotube (Figure S6, Supporting Information). More importantly, when the rate is gradually decreased back to 0.1 A g^{-1} , the capacity can recover to 293 mAh g^{-1} , which could originate from the reactivation process caused by high-rate sodiation.

To explore the underlying reason of the long cycling and ultrafast sodium storage of the $\text{MoSe}_2/\text{P-C}@/\text{TiO}_2$ electrode, the redox pseudocapacitive contribution in the hybrid electrode was examined by separating the capacitive capacity and the diffusion-controlled capacity. The reaction kinetics of the $\text{MoSe}_2/\text{P-C}@/\text{TiO}_2$ nanospheres with Na^+ ions can be investigated by CV profiles at different sweep rates (v) from 0.5 to 2.0 mV s^{-1} . As displayed in Figure 5A, all the CV curves have similar peak shapes except for the corresponding shift during Na^+ insertion/extraction processes. The total stored charges contributed by diffusion-controlled or/and capacitive contributions can be divided using the power law $i = av^b$,^[24,40,49,50] where v is the scan rate, and both a and b are adjustable parameters. Generally, $b = 0.5$ indicates a diffusion-controlled process, and $b = 1.0$ represents capacitive-contributed charge storage. Figure 5B shows the slope of the corresponding $\log(v)$ versus $\log(i)$ plots, in which the b -values are 0.98 and 0.94 for cathodic and anodic peaks, respectively. These values suggest that the two mechanisms coexist in the sodiation/desodiation process, which is mainly controlled by the capacitive process. Moreover, the contributions from the two mechanisms can be estimated from the formula $i(V) = k_1v + k_2v^{1/2}$ at a fixed potential.^[11,49,50] As shown in Figure 5C, 86.2% of the total capacity is attributed to the capacitive contribution at a scan rate of

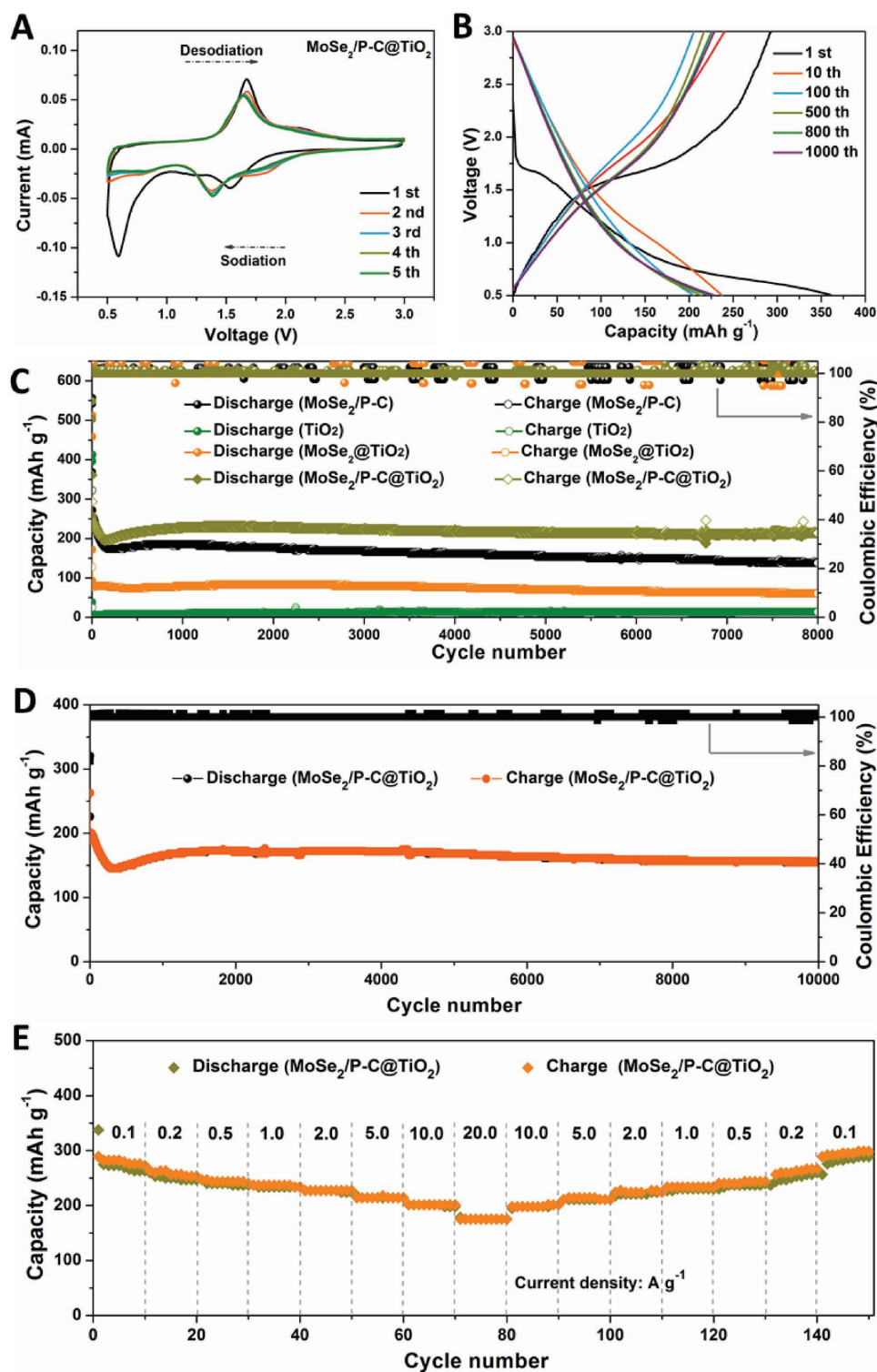


Figure 4. Electrochemical performance of the $\text{MoSe}_2/\text{P-C}@/\text{TiO}_2$ electrode. A) CV curves at a scan rate of 0.1 mV s^{-1} . B) Typical charge–discharge profiles at 5.0 A g^{-1} . C,D) Cycling performance at 5.0 and 10.0 A g^{-1} . E) Rate cycling behavior.

0.5 mV s^{-1} . Along with the sweep rate increases, the capacitance contribution gradually increases, reaching a value of 92.8% at 2.0 mV s^{-1} (Figure 5D). The kinetics analyses obviously manifest the gradual increase of capacity contribution,

where the fast electrochemical kinetics of involved surficial reactions contribute to the high rate capability. The improved Na^+ -reaction kinetics of the $\text{MoSe}_2/\text{P-C}@/\text{TiO}_2$ anode material are further supported by the lower R_{ct} than that of the

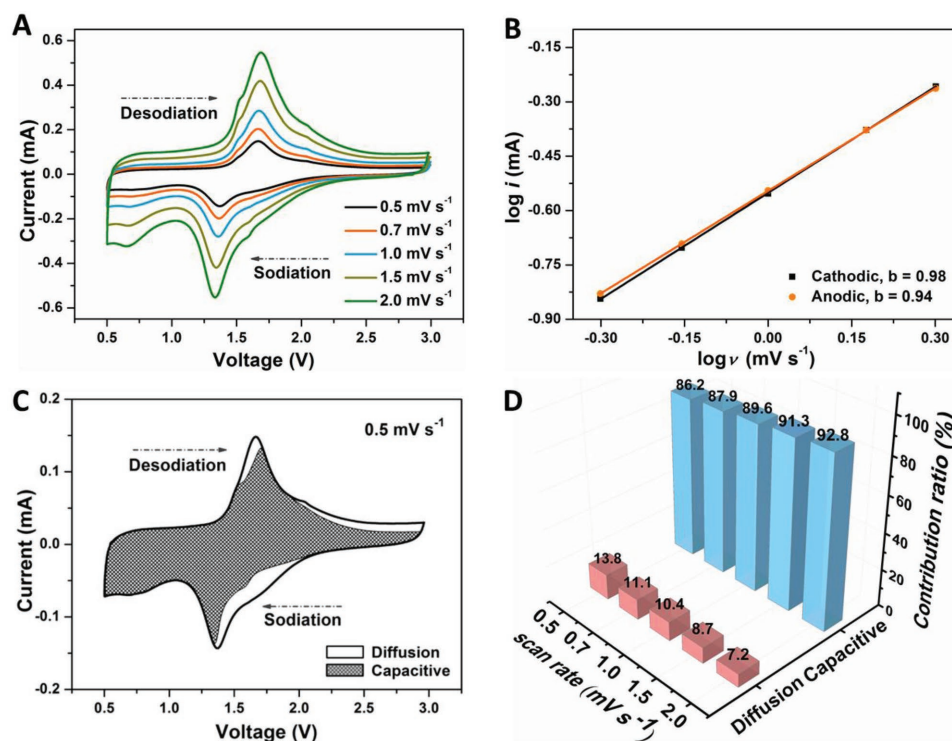


Figure 5. Kinetics analysis of the sodium storage behavior for the MoSe₂/P-C@TiO₂ electrode. A) CV curves at different scan rates. B) *b*-value analysis based on the relationship between the peak currents and the scan rates. C) Capacitive (shade region) and diffusion-controlled charge storage contributions for the CV curve at scan rate of 0.5 mV s⁻¹. D) Contribution ratio of the capacitive and diffusion-controlled charges at different scan rates.

MoSe₂/P-C electrode (Figure S7A, Supporting Information) and the decreasing charge-transfer resistance upon cycling (Figure S7B, Supporting Information). Postmortem study verifies that the structure of the MoSe₂/P-C@TiO₂ hybrid spheres can be well retained after 1000 cycles at a current density of 5.0 A g⁻¹ (Figure S8, Supporting Information). This confirms TiO₂ coating can relieve structural collapse and promote ultralong cycling stability.

In view of the superior sodium-storage performance of MoSe₂/P-C@TiO₂ in a half cell, full cells are further assembled with homemade Na₃V₂(PO₄)₃@C (NVP@C) as the cathode material to evaluate its potential for practical application. The homemade NVP@C was synthesized by a hydrothermal assisted sol-gel method,^[51] which has good phase purity and crystal structure as shown in Figure S9A (Supporting Information). When used as cathode material for a half cell, it exhibits a capacity of 80.8 mAh g⁻¹ at 200 mA g⁻¹ after 100 cycles and shows a flat voltage plateau around 3.4 V (Figure S9B,C, Supporting Information), which is consistent with previous reports.^[9,26,52] For a sodium-ion full battery, a discharge voltage plateau around 1.85 V can be seen from the galvanostatic discharge-charge curves at 0.5 A g⁻¹ in the voltage range of 0.5–3.0 V (Figure S10A, Supporting Information). Figure S10B (Supporting Information) shows the cycling stability of the MoSe₂/P-C@TiO₂//NVP@C full cells at current density of 500 mA g⁻¹. A reversible capacity of 242.2 mAh g⁻¹ can be maintained after 100 cycles with the CE over 99%, suggesting a robust cyclability of MoSe₂/P-C@TiO₂ when applied into full cells.

3. Conclusion

In conclusion, a facile self-templating strategy has been developed to synthesize PPy-PMo₁₂@TiO₂ nanospheres using PPy-PMo₁₂ as the precursor via a hydrolysis reaction. Through a subsequent simultaneous selenization-carbonization process, MoSe₂/P-C@TiO₂ hybrid nanospheres can be easily achieved. Benefiting from the unique structural and multicompositional features, the MoSe₂/P-C@TiO₂ hybrid nanospheres provide superior sodium-storage performance based on high capacity, excellent cycling stability, and exceptional rate capability. Specifically, the MoSe₂/P-C@TiO₂ hybrid nanospheres deliver a reversible capacity of 214 mAh g⁻¹ at 5.0 A g⁻¹ for 8000 cycles and 154 mAh g⁻¹ at 10.0 A g⁻¹ for 10000 cycles as well as an ultrahigh rate capability up to 20.0 A g⁻¹ with a capacity of 175 mAh g⁻¹. This work could open up a new avenue to design and prepare complex multicompositional hybrids toward various applications.

4. Experimental Section

Synthesis of PPy-PMo₁₂ Precursor: According to a previous report,^[47] the synthetic method is as follows. Pyrrole solution (420 μL in 25 mL of absolute ethanol) was added dropwise to an aqueous solution of phosphomolybdic acid (H₃PMo₁₂O₄₀·xH₂O, 2.19 g in 100 mL of deionized H₂O). After the mixture was continuously stirred at room temperature for 12 h and then aged for 24 h, the product was obtained through centrifugation, washed with deionized H₂O and absolute ethanol several times, and then dried at 60 °C. The PPy-PMo₁₂ precursor was collected for further use.

Synthesis of MoSe₂/P-C@TiO₂ Nanospheres: In a typical procedure,^[35] first, 200 mg of the above PPy-PMo₁₂ precursor was dispersed in 96.7 mL 0.1 M HCl solution which contains 2 g dihydroxybis (ammonium lactato) titanium (IV) (50 wt% solution in H₂O) under magnetic stirring at room temperature for 2 h. The PPy-PMo₁₂@TiO₂ nanoparticles were collected by centrifugation, washed with deionized H₂O and absolute ethanol several times, and then dried at 60 °C. The PPy-PMo₁₂@TiO₂ (100 mg) was placed in a porcelain boat at the downstream side of the furnace with 200 mg of Se powder placed another boat at the upstream side in the tube furnace. Eventually, the MoSe₂/P-C@TiO₂ nanospheres were obtained after heated at 700 °C with a scan rate of 1 °C min⁻¹ in a H₂/Ar flow for 2 h. The MoSe₂/P-C nanospheres were prepared in the same condition except the TiO₂ coating. And TiO₂ was prepared in a similar procedure to MoSe₂/P-C@TiO₂ except the addition of PPy-PMo₁₂ precursor and calcination with Se powder. MoSe₂@TiO₂ was prepared using a similar procedure to MoSe₂/P-C@TiO₂ except the calcination of PPy-PMo₁₂ at 600 °C in air before calcination with Se powder in order to remove the carbon source of PPy.

Materials Characterizations: XRD patterns were performed on a Rigaku Ultima IV X-Ray Diffractometer. FESEM images were recorded by a scanning electron microscope (Philips XL30 FEG SEM). TEM, HRTEM, and HAADF-STEM images were collected on FEI Talos F200X TEM at 200 kV. Raman spectra were carried out on a HORIBA Evolution Ramanscope with the excitation wavelength of 532 nm. TGA was carried out using PerkinElmer TGA 7 in an air atmosphere with a heating rate of 10 °C min⁻¹. XPS was measured by Thermo ESCALAB 250 surface analysis system. The N₂ adsorption-desorption isothermal curve and the BET surface area was calculated via Micro ASAP2020 at 77 K.

Electrochemical Measurements: The performances of sodium storage were evaluated by coin cells (CR2032) assembled in an Ar glovebox with a voltage window of 0.5–3.0 V. The sodium metal, glass fiber, and 1.0 M NaCF₃SO₃ solution in diethyleneglycoldimethylether (DEGDME) played the parts of counter electrode, separator, and electrolyte, respectively. The working electrode was prepared by forming a H₂O-based slurry composed of active material, carbon black, and sodium carboxymethyl cellulose (CMC) with a weight ratio of 6:2:2 on a copper foil. Then the coated foil was dried at 80 °C and cut into 12 mm discs with a loading of ≈1.0 mg cm⁻². CV curves and electrochemical impedance spectroscopy (EIS) were performed using a Gamry 30115 electrochemical workstation with different scan rates from 0.5 to 2.0 mV s⁻¹ and frequencies of 0.1 MHz to 10 mHz. Galvanostatic discharge/charge cycling was carried out using Neware-5 V10 mA system (Shenzhen Xinwei). For Na-ion full cells, the cathode was made of homemade Na₃V₂(PO₄)₃@C, carbon black, and poly(vinylidene fluoride) (PVDF) were mixed in N-methyl-2-pyrrolidone (NMP) with a weight ratio of 8:1:1 to form a slurry which was coated on an aluminum foil.

Supporting Information

Supporting Information is available from the Wiley Online Library or from the author.

Acknowledgements

This work was financially supported by the National Natural Science Foundation of China (NSFC Grant Nos. 21571187 and 51702366), Taishan Scholar Foundation (ts201511019), Natural Science Foundation of Shandong Province (ZR2017BB046), and the Fundamental Research Funds for the Central Universities (17CX02037A and 18CX02047A).

Conflict of Interest

The authors declare no conflict of interest.

Keywords

anode materials, interlayer-expanded MoSe₂ nanospheres, phosphorus-doped carbon, sodium-ion batteries, TiO₂ coating layer

Received: July 29, 2018

Revised: September 20, 2018

Published online:

- [1] L. Xiao, Y. Cao, W. A. Henderson, M. L. Sushko, Y. Shao, J. Xiao, W. Wang, M. H. Engelhard, Z. Nie, J. Liu, *Nano Energy* **2016**, *19*, 279.
- [2] S. Y. Hong, Y. Kim, Y. Park, A. Choi, N.-S. Choi, K. T. Lee, *Energy Environ. Sci.* **2013**, *6*, 2067.
- [3] Y. Liu, N. Zhang, C. Yu, L. Jiao, J. Chen, *Nano Lett.* **2016**, *16*, 3321.
- [4] M. D. Slater, D. Kim, E. Lee, C. S. Johnson, *Adv. Funct. Mater.* **2013**, *23*, 947.
- [5] J. Yang, X. Zhou, D. Wu, X. Zhao, Z. Zhou, *Adv. Mater.* **2017**, *29*, 1604108.
- [6] L. Ling, Y. Bai, Z. Wang, Q. Ni, G. Chen, Z. Zhou, C. Wu, *ACS Appl. Mater. Interfaces* **2018**, *10*, 5560.
- [7] H. Park, J. Kwon, H. Choi, D. Shin, T. Song, X. W. D. Lou, *ACS Nano* **2018**, *12*, 2827.
- [8] R. Sun, S. Liu, Q. Wei, J. Sheng, S. Zhu, Q. An, L. Mai, *Small* **2017**, *13*, 1701744.
- [9] J. Deng, Q. Gong, H. Ye, K. Feng, J. Zhou, C. Zha, J. Wu, J. Chen, J. Zhong, Y. Li, *ACS Nano* **2018**, *12*, 1829.
- [10] W. Kang, Y. Wang, J. Xu, *J. Mater. Chem. A* **2017**, *5*, 7667.
- [11] F. Niu, J. Yang, N. Wang, D. Zhang, W. Fan, J. Yang, Y. Qian, *Adv. Funct. Mater.* **2017**, *27*, 1700522.
- [12] M. Zhu, Z. Luo, A. Pan, H. Yang, T. Zhu, S. Liang, G. Cao, *Chem. Eng. J.* **2018**, *334*, 2190.
- [13] D. Xie, X. Xia, Y. Zhong, Y. Wang, D. Wang, X. Wang, J. Tu, *Adv. Energy Mater.* **2017**, *7*, 1601804.
- [14] J. Zhang, W. Kang, M. Jiang, Y. You, Y. Cao, T.-W. Ng, D. Y. W. Yu, C.-S. Lee, J. Xu, *Nanoscale* **2017**, *9*, 1484.
- [15] Y. N. Ko, S. H. Choi, S. B. Park, Y. C. Kang, *Nanoscale* **2014**, *6*, 10511.
- [16] J. Li, H. Hu, F. Qin, P. Zhang, L. Zou, H. Wang, K. Zhang, Y. Lai, *Chem. - Eur. J.* **2017**, *23*, 14004.
- [17] D. Xie, W. Tang, Y. Wang, X. Xia, Y. Zhong, D. Zhou, D. Wang, X. Wang, J. Tu, *Nano Res.* **2016**, *9*, 1618.
- [18] Z. Zhang, X. Yang, Y. Fu, K. Du, *J. Power Sources* **2015**, *296*, 2.
- [19] J. Zhang, M. Wu, T. Liu, W. Kang, J. Xu, *J. Mater. Chem. A* **2017**, *5*, 24859.
- [20] X. Yang, Z. Zhang, Y. Fu, Q. Li, *Nanoscale* **2015**, *7*, 10198.
- [21] Y. Tang, Z. Zhao, Y. Wang, Y. Dong, Y. Liu, X. Wang, J. Qiu, *ACS Appl. Mater. Interfaces* **2016**, *8*, 32324.
- [22] S. H. Choi, Y. C. Kang, *Nanoscale* **2016**, *8*, 4209.
- [23] H. Liu, H. Guo, B. Liu, M. Liang, Z. Lv, K. R. Adair, X. Sun, *Adv. Funct. Mater.* **2018**, *28*, 1707480.
- [24] B. Li, B. Xi, Z. Feng, Y. Lin, J. Liu, J. Feng, Y. Qian, S. Xiong, *Adv. Mater.* **2018**, *30*, 1705788.
- [25] J. Ni, S. Fu, Y. Yuan, L. Ma, Y. Jiang, L. Li, J. Lu, *Adv. Mater.* **2018**, *30*, 1704337.
- [26] L. Yu, J. Liu, X. Xu, L. Zhang, R. Hu, J. Liu, L. Ouyang, L. Yang, M. Zhu, *ACS Nano* **2017**, *11*, 5120.
- [27] Y. Xu, E. M. Lotfabad, H. Wang, B. Farbod, Z. Xu, A. Kohandehghan, D. Mitlin, *Chem. Commun.* **2013**, *49*, 8973.
- [28] D. Su, S. Dou, G. Wang, *Chem. Mater.* **2015**, *27*, 6022.
- [29] L. Ling, Y. Bai, Y. Li, Q. Ni, Z. Wang, F. Wu, C. Wu, *ACS Appl. Mater. Interfaces* **2017**, *9*, 39432.

- [30] Y. Fu, Q. Wei, X. Wang, H. Shu, X. Yang, S. Sun, *J. Mater. Chem. A* **2015**, *3*, 13807.
- [31] X. Zhang, H. Chen, Y. Xie, J. Guo, *J. Mater. Chem. A* **2014**, *2*, 3912.
- [32] W. Ren, W. Zhou, H. Zhang, C. Cheng, *ACS Appl. Mater. Interfaces* **2017**, *9*, 487.
- [33] X. Wang, Q. Xiang, B. Liu, L. Wang, T. Luo, D. Chen, G. Shen, *Sci. Rep.* **2013**, *3*, 2007.
- [34] H.-E. Wang, X. Zhao, X. Li, Z. Wang, C. Liu, Z. Lu, W. Zhang, G. Cao, *J. Mater. Chem. A* **2017**, *5*, 25056.
- [35] G. Huang, F. Zhang, X. Du, J. Wang, D. Yin, L. Wang, *Chem. - Eur. J.* **2014**, *20*, 11214.
- [36] Z.-T. Shi, W. Kang, J. Xu, Y.-W. Sun, M. Jiang, T.-W. Ng, H.-T. Xue, D. Y. W. Yu, W. Zhang, C.-S. Lee, *Nano Energy* **2016**, *22*, 27.
- [37] J. Zhang, M. Li, Z. Feng, J. Chen, C. Li, *J. Phys. Chem. B* **2006**, *110*, 927.
- [38] R. Wei, X. Tian, Z. Hu, H. Zhang, T. Qiao, X. He, Q. Chen, Z. Chen, J. Qiu, *Opt. Express* **2016**, *24*, 25337.
- [39] X. Wang, K. Chen, G. Wang, X. Liu, H. Wang, *ACS Nano* **2017**, *11*, 11602.
- [40] C. Zhao, C. Yu, M. Zhang, Q. Sun, S. Li, M. Norouzi Banis, X. Han, Q. Dong, J. Yang, G. Wang, X. Sun, J. Qiu, *Nano Energy* **2017**, *41*, 66.
- [41] Z. Xu, H. Wang, Z. Li, A. Kohandehghan, J. Ding, J. Chen, K. Cui, D. Mitlin, *J. Phys. Chem. C* **2014**, *118*, 18387.
- [42] S. Lei, X. Wang, B. Li, J. Kang, Y. He, A. George, L. Ge, Y. Gong, P. Dong, Z. Jin, G. Brunetto, W. Chen, Z. Lin, R. Baines, D. S. Galvão, J. Lou, E. Barrera, K. Banerjee, R. Vajtai, P. Ajayan, *Nat. Nanotechnol.* **2016**, *11*, 465.
- [43] Q. Xiao, J. Zhang, C. Xiao, Z. Si, X. Tan, *Sol. Energy* **2008**, *82*, 706.
- [44] Y. Luo, J. Luo, J. Jiang, W. Zhou, H. Yang, X. Qi, H. Zhang, H. J. Fan, D. Y. W. Yu, C. M. Li, T. Yu, *Energy Environ. Sci.* **2012**, *5*, 6559.
- [45] D. Wang, Y. Wang, X. Li, Q. Luo, J. An, J. Yue, *Catal. Commun.* **2008**, *9*, 1162.
- [46] X. Sun, C. Brückner, Y. Lei, *Nanoscale* **2015**, *7*, 17278.
- [47] Y.-Y. Chen, Y. Zhang, W.-J. Jiang, X. Zhang, Z. Dai, L.-J. Wan, J.-S. Hu, *ACS Nano* **2016**, *10*, 8851.
- [48] L. Pan, X.-D. Zhu, X.-M. Xie, Y.-T. Liu, *Adv. Funct. Mater.* **2015**, *25*, 3341.
- [49] X. Xu, J. Liu, J. Liu, L. Ouyang, R. Hu, H. Wang, L. Yang, M. Zhu, *Adv. Funct. Mater.* **2018**, *28*, 1707573.
- [50] J. Wang, J. Polleux, J. Lim, B. Dunn, *J. Phys. Chem. C* **2007**, *111*, 14925.
- [51] W. Duan, Z. Zhu, H. Li, Z. Hu, K. Zhang, F. Cheng, J. Chen, *J. Mater. Chem. A* **2014**, *2*, 8668.
- [52] Y. Fang, L. Xiao, X. Ai, Y. Cao, H. Yang, *Adv. Mater.* **2015**, *27*, 5895.